Optimal external forces of the lock-in phenomena for flow past an inclined plate in uniform flow

Makoto Iima *

Graduate School of Integrated Life Sciences, Hiroshima University, 1-7-1, Kagamiyama Higashihiroshima, Hiroshima 739-8521, Japan

(Received 2 November 2023; accepted 4 March 2024; published 2 April 2024)

We theoretically studied the optimal control, frequency lock-in, and phase lock-in phenomena due to the spatially localized periodic forcing in flow past an inclined plate. Although frequency lock-in is evident in many fluid phenomena, especially fluid-structure interactions, not many researchers have investigated it using a theoretical approach based on flow details. We obtained detailed information on the lock-in phenomena to external periodic forcing using phase reduction theory, a mathematical method for extracting the dynamics near the limit cycle. Furthermore, the optimal forces applied to the velocity field were determined under the condition of the minimum forcing energy and maximum lock-in range. The study of uniform periodic forces applied within spatially confined regions led to the conclusion that the effective lock-in position, which includes both the upstream and downstream areas of the plate, depends on the principal frequency of the force. The frequency lock-in range of these forces was analyzed and compared with theoretical predictions.

DOI: 10.1103/PhysRevE.109.045102

I. INTRODUCTION

Effective flow control is demanded in many research areas, e.g., fluid engineering, nonlinear physics, and environmental research. In particular, the frequency lock-in and the phase lock-in under external periodic forcing have been investigated in the context of fluid-structure interactions. Examples of such interactions are spring-suspended airfoils in transonic flows in terms of aircraft vibration due to the shock wave oscillation [1,2], spring-suspended cylinders exerted by random waves in terms of fatigue and failures of structures in offshore systems [3], and various problems in flow-induced vibrations [4,5].

When an external periodic force is applied, the lock-in details can be provided through laboratory experiments and time evolution of computational fluid dynamics. It has been, however, difficult to determine the optimal form of the external force to achieve the lock-in phenomena even if the forces are weak, as it requires complete information of the flow response to external perturbations. Thus, it would be very helpful if we could design the external force to be considered as a control input.

A mathematical tool called phase reduction theory can be used for this purpose. It can be applied to a dynamical system with a limit cycle (LC) and describes the essential dynamics near the LC. The reduced equation (called phase equation) has few degrees of freedom [6]. Phase reduction theory has been successfully applied to various rhythmic phenomena [7] in mechanical vibration (synchronization of metronomes [8]), ethology (synchronization of flashing fireflies [9,10]), biology (circadian rhythms [11,12]), etc. Compared with the applications in mechanical engineering and life sciences, its applications to fluid mechanics are under development; e.g., thermal convection [13,14], Kármán's vortex streets [15–21], wake on a wing [20–23], and other phenomena [24–27]. We note that periodic vortex shedding is observed past inclined wings when the Reynolds number is $O(10^2)$ [28].

In phase reduction theory, complete information of the phase response can be obtained from the phase sensitivity function (PSF) [6,29]. Thus far, three techniques have been proposed to calculate the PSF, i.e., the direct method [15,17–20], the adjoint method [13,14], and the Jacobian-free projection method [16,22,30]. The theoretical background of these methods can be found in Refs. [22,29].

The direct method measures the phase shift due to perturbation by time evolution and is suitable for cases where phase shifts due to a small number of degrees of freedom are of interest. However, the accuracy of the phase-shift measurement is limited by the time step of the numerical calculation and requires a sufficiently long time for convergence. The adjoint method obtains the PSF using time evolution of the adjoint equation derived from the equation. This provides a convenient computational procedure, although the derivation of the adjoint equation is not always possible. The Jacobian-free projection method can be used to obtain the PSF by computing the eigenvector of the matrix constructed by time evolution alone. It can be applied to the system from which the adjoint equation is difficult to derive, although the limit cycle solution is required and the computational cost is higher than the adjoint method (yet lower than the direct method).

In the lock-in phenomena due to the periodic external forcing, the phase reduction theory can provide predictions, such as the frequency range of the external forcing for the frequency lock-in and the phase difference for the phase lock-in [29]. Furthermore, the optimal form of the external forcing under various conditions can be calculated as a constrained optimization problem [31–35]. The optimal forms of the external forcing for Kámán vortex streets were studied. Khodokar and Taira calculated the largest lock-in region for

*iima@hiroshima-u.ac.jp

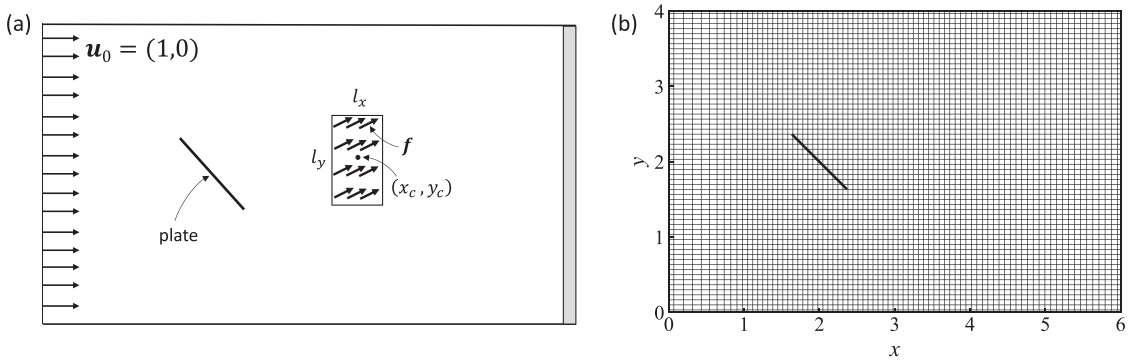

FIG. 1. (a) Model configuration. An inclined plate is placed in the wind tunnel. A uniform external force was applied within a rectangular area of size $l_x \times l_y$ centered at (x_c, y_c). (b) Computational grid and the plate model. Grid lines are drawn on every other line for visibility.

a sinusoidal form $1 + \sin \Omega t$ applied at a single point. They found that the best point to be near the separation point [17]. Khodokar *et al.* studied the case where the cylinder is moving in uniform flow [18]. Loe *et al.* studied the synchronization between the wake behind a two-dimensional (2D) cylinder in a tube and the vibration of elastic walls in a sinusoidal form [19]. The lock-in region was maximized when the perturbation occurred near the downstream end of the cylinder.

Here, we considered the optimal forcing of the temporally periodic form applied uniformly to a spatially confined region. Based on the spatial distributions of the PSF for both the cylinder and the plate [22,36], the phase shift property due to perturbation has a complex spatiotemporal structure. This fact implies that the practical control of the flow based on simple control inputs, e.g., spatially uniform input within a confined area and a temporally simple (e.g., sinusoidal) function rather than an optimized waveform, may provide us different lock-in properties from the optimized input by a pointwise designable function. Such a study will provide insights into the appropriate region and frequency, especially for fluid engineering.

In this study, we investigated the lock-in phenomena of the flow past the inclined plate in a wind tunnel in two-dimensional space. First, we analyzed the qualitative characteristics of the PSF, which are useful for designing the control input. Specifically, the details of the phase response to the external forces were described by using temporal Fourier decomposition of PSF, which has not been used so far. These results were used to tackle the lock-in problem for a uniform periodic external force within a confined region. We aimed to answer the following questions:

(1) Where is the optimum region for the lock-in?

(2) How does this position depend on the principal frequency and the direction of the force?

We showed that the optimal position depends on the principal frequency and the direction of the force. The optimal position may be away from the surface of the plate. These results were compared with the theoretical prediction, which provides the maximum lock-in range under the constant energy of a external force and the minimum energy.

II. METHOD

A. Fluid dynamics

The flow past a flat plate in a wind tunnel in two-dimensional space [Fig. 1(a)] was considered. The flow is governed by the incompressible Navier-Stokes equations in a nondimensional form:

$$\frac{\partial \boldsymbol{u}}{\partial t} + \boldsymbol{u} \cdot \nabla \boldsymbol{u} = -\nabla p + \frac{1}{\mathrm{Re}} \Delta \boldsymbol{u} + \boldsymbol{f}(\boldsymbol{x}, \Omega t), \quad \nabla \cdot \boldsymbol{u} = \boldsymbol{0}, \tag{1}$$

where $\boldsymbol{u} = (u, v)$ denotes the velocity, p denotes the pressure, and Re denotes the Reynolds number. The time-periodic external force is denoted by $\boldsymbol{f} = (f_x, f_y)$ and the angular frequency is denoted by Ω. The uniform flow is represented by $\boldsymbol{u}_0 = (u_0, v_0) = (1, 0)$. The system was assumed to be in a tunnel of width $4c$, where c (=1) is the cord of the plate. The system is nondimensionalized by c as the length scale and c/u_0 as the timescale; $\mathrm{Re} = u_0 c/\nu$, where ν is the kinematic viscosity.

The computational domain was $[0, 6c] \times [0, 4c]$ to reduce the computational cost of calculating the functions describing the detailed phase response to an external force [Fig. 1(b)].

The following boundary conditions were applied: A constant velocity $\boldsymbol{u}_0$ was applied at the domain boundaries $x = 0$, $y = 0$, and $y = 4c$. The outflow boundary condition proposed by Dong *et al.* [37], which aims at minimizing the domain truncation, was applied at the boundary $x = 6c$.

In the following sections, the optimal external forces were considered. In addition to the optimal forces predicted by the phase reduction theory (Secs. II C 1 and II C 2), the optimal position was considered to maximize the frequency lock-in region under the condition of uniform external force within a rectangle of size $l_x \times l_y$ centered at (x_c, y_c) [Fig. 1(a)].

To solve Eq. (1), a fractional step method was used. The finite-volume method was used for spatial discretization [38]. The Adams–Bashforth scheme and the Crank–Nicolson scheme were used for time integration of the advection terms and that of the dissipation terms, respectively. The flat plate was represented by an immersed boundary method [39]. The computational code was the same as that used in Ref. [22].

The center of the plate was set to $(x, y) = (2c, 2c)$ and the angle of attack (AoA) was set to $\pi/4$. The Reynolds number Re was set to 200. An unequal and orthonormal grid was used, although the grid spacing in the region around the plate was uniform at $c/30$ [Fig. 1(b)]. The number of grid points was $n_x \times n_y$ where $n_x = 160$ and $n_y = 120$. In this setup, the periodic flow was achieved and phase reduction theory can be applied.

The calculation scheme was compared with the spectral element method, in which the computational domain was divided into quadrilateral elements, and physical quantities were represented using the spectral method [40]; their results agreed reasonably well with each other (Appendix A). In addition, we concluded that the phase sensitivity vector (see Sec. II B) near the plate was less sensitive to the size of the wind tunnel (Appendix B).

The periodic solution without external force was obtained numerically using the Newton–Raphson method [41] under the condition where the relative errors of both the residue and the increment of the iteration were less than 10^{-10}. The period was $T = 3.439\,58$ when a single period was segmented into $1408 = 2^7 \times 11$ time steps. The origin of the phase was set as the time at which the maximum lift was attained.

The Jacobian-free projection method [22] was used to obtain the projected phase-sensitivity function. In this calculation, we focused on the response to the perturbation of the velocity components, $\boldsymbol{u} = (u, v)$ alone, whereas the responses to the pressure and variables in previous time steps were not calculated. The Ritz value, an indicator for the convergence of the projection field [22], was 6.59×10^{-3} at the origin of the phase, which was reasonably small for the analysis.

B. Phase reduction theory

We analyzed an autonomous dynamical system with an external periodic force $\boldsymbol{F}(\Omega t)$:

$$\frac{d\boldsymbol{X}}{dt} = \boldsymbol{G}(\boldsymbol{X}) + \boldsymbol{F}(\Omega t), \tag{2}$$

where $\boldsymbol{X} \in \mathbb{R}^M$ is the state in the M-dimensional phase space, $\boldsymbol{G}$ determines the autonomous dynamics system, and $\boldsymbol{F}(\Omega t)$ is the time-periodic external force with angular frequency Ω and period $T = 2\pi/\Omega$, i.e., $\boldsymbol{F}(\Omega(t+T)) = \boldsymbol{F}(\Omega t)$. We assumed a weak external force to apply phase reduction theory. According to the phase reduction theory [6,7], the phase equation derived from Eq. (2) reads

$$\frac{d\phi}{dt} = \omega + \boldsymbol{Z}(\phi) \cdot \boldsymbol{F}(\Omega t), \tag{3}$$

where $\phi \in [0, 2\pi)$ is the phase, ω is the natural frequency, and $\boldsymbol{Z}(\phi)$ is the phase sensitivity function.

We related $\boldsymbol{X}$ to the flow field data. Suppose that the space is discretized by $n_x \times n_y$, the position $\boldsymbol{x} = (x, y)$ can be labeled by $n(= n_x n_y)$ indices $\boldsymbol{x}_1, \ldots, \boldsymbol{x}_n$. In the same way, the velocity field (u, v) is discretized to construct $\boldsymbol{X}$ as

$$\boldsymbol{X} = (u_1, \ldots, u_n, v_1, \ldots, v_n) \quad (M = 2n), \tag{4}$$

where u_j and v_j are the values of u and v at $\boldsymbol{x} = \boldsymbol{x}_j$, respectively. The external force applied to the fluid $\boldsymbol{f}(\boldsymbol{x}, \Omega t)$ is related to $\boldsymbol{F}(\Omega t)$ as

$$\begin{aligned}\boldsymbol{F}(\Omega t) = (&f_u(\boldsymbol{x}_1, \Omega t), \ldots, f_u(\boldsymbol{x}_n, \Omega t),\\ &f_v(\boldsymbol{x}_1, \Omega t), \ldots, f_v(\boldsymbol{x}_n, \Omega t)).\end{aligned} \tag{5}$$

In the formal calculation, $\boldsymbol{X}$ contains more variables, the pressure p, and the variables that used in the numerical algorithm when the multistep method is used for time evolution (cf. Sec. II A, Ref. [22]).

The phase sensitivity vector, $\boldsymbol{q}(\boldsymbol{x}, \phi) = (q_u(\boldsymbol{x}, \phi), q_v(\boldsymbol{x}, \phi))$, describes the phase shift due to the unit force at the position $\boldsymbol{x}$ at the phase ϕ. The phase shift due to the perturbation $\Delta\boldsymbol{u}\,\delta(\boldsymbol{x} - \boldsymbol{x}_0)$, where $\Delta\boldsymbol{u}$ and $\delta(\boldsymbol{x})$ represent a constant perturbation vector and the three-dimensional δ function, respectively, is expressed as $\Delta\boldsymbol{u} \cdot \boldsymbol{q}(\boldsymbol{x}_0)$ [16].

The relationship between $\boldsymbol{q}(\boldsymbol{x}, \phi)$ and $\boldsymbol{Z}(\phi)$ is

$$\begin{aligned}\boldsymbol{Z}(\phi) = (&q_u(\boldsymbol{x}_1, \phi)\Delta S_1, \ldots, q_u(\boldsymbol{x}_n, \phi)\Delta S_n,\\ &q_v(\boldsymbol{x}_1, \phi)\Delta S_1, \ldots, q_v(\boldsymbol{x}_n, \phi)\Delta S_n),\end{aligned} \tag{6}$$

where ΔS_j $(j = 1, \ldots, n)$ is the area allocated for the grid point $\boldsymbol{x} = \boldsymbol{x}_j$.

When the external force $\boldsymbol{F}(\Omega t)$ is weak, the phase equation is reduced to the following equation by the averaging over one period [6,29]:

$$\frac{d\psi}{dt} = \Delta\omega + \Gamma(\psi), \tag{7}$$

$$\Gamma(\psi) = \frac{1}{2\pi}\int_0^{2\pi} \boldsymbol{Z}(\theta + \psi) \cdot \boldsymbol{F}(\theta) d\theta [= \langle \boldsymbol{Z}(\theta + \psi) \cdot \boldsymbol{F}(\theta) \rangle], \tag{8}$$

where $\psi = \phi - \Omega t$ is the phase difference between the system and the external force, and $\Delta\omega = \omega - \Omega$ is the frequency difference. The function $\Gamma(\psi)$ is called the phase coupling function.

Scaling of variables in relation to the level of discretization, denoted n, is examined below. As both $q_i(\boldsymbol{x}_j, \phi)$ and $f_i(\boldsymbol{x}_j, \Omega t)$ $(i = u, v;\ j = 1, \ldots, n)$ are independent of n, Eqs. (6) and (8) imply that $\boldsymbol{Z}(\phi) \simeq S/n \sim n^{-1}$ and $\Gamma(\psi) \sim n^0$, where $S = l_x l_y = \sum_{k=1}^n \Delta S_k$. Therefore, the magnitude of $\boldsymbol{Z}(\phi)$ depends on the value of n while $\Gamma(\phi)$ remains constant in the current formulation.

Equation (7) implies that the frequency lock-in occurs when

$$\begin{aligned}&\Gamma_{\min} < \Delta\omega < \Gamma_{\max},\\ &\Gamma_{\min} = \min_{0 \leqslant \psi < 2\pi} \Gamma(\psi),\\ &\Gamma_{\max} = \max_{0 \leqslant \psi < 2\pi} \Gamma(\psi).\end{aligned} \tag{9}$$

For later convenience, we define

$$\psi_+ = \arg\max\Gamma(\psi), \quad \psi_- = \arg\min\Gamma(\psi). \tag{10}$$

For further analysis, we decompose $\boldsymbol{f}(\boldsymbol{x}, \Omega t)$ and $\boldsymbol{q}(\boldsymbol{x}, \omega t)$ into Fourier series:

$$\begin{aligned}\boldsymbol{f}(\boldsymbol{x}, \Omega t) &= \sum_{m=-\infty}^{\infty} \tilde{\boldsymbol{f}}(\boldsymbol{x}; m) e^{im\Omega t},\\ \boldsymbol{q}(\boldsymbol{x}, \omega t) &= \sum_{m=-\infty}^{\infty} \tilde{\boldsymbol{q}}(\boldsymbol{x}; m) e^{im\omega t},\end{aligned} \tag{11}$$

where $\tilde{\boldsymbol{f}}$ and $\tilde{\boldsymbol{q}}$ are Fourier components of $\boldsymbol{f}$ and $\boldsymbol{q}$, respectively. Similarly, we decomposed $\boldsymbol{F}(\phi)$ and $\boldsymbol{Z}(\phi)$ into Fourier series:

$$\boldsymbol{F}(\phi) = \sum_{m=-\infty}^{\infty} \tilde{\boldsymbol{F}}(m) e^{im\phi}, \quad \boldsymbol{Z}(\phi) = \sum_{m=-\infty}^{\infty} \tilde{\boldsymbol{Z}}(m) e^{im\phi}. \tag{12}$$

Subsequently, Eq. (8) provided the expression of $\Gamma(\psi)$ as

$$\Gamma(\psi) = \sum_{m=-\infty}^{\infty} \tilde{\boldsymbol{Z}}(m) \cdot \tilde{\boldsymbol{F}}^*(m) e^{im\psi}, \tag{13}$$

where * represents the complex conjugate. Equation (13) indicates that $\tilde{\boldsymbol{Z}}(m)$ determines the response to the mth mode of external force, $\tilde{\boldsymbol{F}}^*(m)$. In Sec. III, we discuss spatial distribution of strong-response region for the external forces with different modes in detail.

For $\boldsymbol{F}(t) = \epsilon \boldsymbol{F}_0 \sin(kt)$, $\Gamma(\psi) = -\epsilon |\boldsymbol{F}_0 \cdot \tilde{\boldsymbol{Z}}(k)| \sin(k\psi + \varphi)$, where $\varphi = \arg(\boldsymbol{F}_0 \cdot \tilde{\boldsymbol{Z}}(k))$. Consequently, $\Gamma_{\max} = \epsilon |\boldsymbol{F}_0 \cdot \tilde{\boldsymbol{Z}}(k)|$. Furthermore, if certain components of $\boldsymbol{F}_0$ are zero, the corresponding components of $\tilde{\boldsymbol{Z}}(m)$ do not contribute to $\Gamma(\psi)$, which directly follows from Eqs. (12) and (13).

Here, we consider a specific case which will be useful for the following analysis (Sec. III B). We assume that (1) the components of $\boldsymbol{F}_0$ are the same, i.e., $\boldsymbol{F}_0 = (f_0, \ldots, f_0)$ (f_0 is a constant). (2) The amplitude of the component of $\tilde{\boldsymbol{Z}}(k)$ are the same, while the arguments are not in general, i.e., $\tilde{\boldsymbol{Z}}(k) = (z(k)e^{i\theta_1}, z(k)e^{i\theta_2}, \ldots, z(k)e^{i\theta_n})$ [$z(k)$ is a constant and θ_j is an argument]. Then, we have

$$\Gamma_{\max} = \epsilon |f_0| z(k) \left| \sum_{j=1}^{n} \exp\left(i\theta_j\right) \right| \leqslant \epsilon n |f_0| z(k), \tag{14}$$

where the last equality holds when θ_j is independent of j. Geometrically, the condition implies that the vectors representing the components of $\tilde{\boldsymbol{Z}}(k)$ in the complex plane are parallel. Similar analyses can be applied in the case that certain components of $\boldsymbol{F}_0$ are zero.

C. Optimal external forces under several conditions

1. Case A: Minimum energy that enables lock-in phenomena

We considered an external force with minimum energy under the constraint of the lock-in phenomenon based on Ref. [32]. To obtain the optimal force, we minimize the Lagrangian function $J_{\pm}[\boldsymbol{F}] = \langle |\boldsymbol{F}|^2 \rangle - \lambda[\Delta\omega + \Gamma(\psi_{\pm})]$. A straightforward calculation provides the minimizers $\boldsymbol{F}_{\pm}$ for $J_{\pm}$ as

$$\boldsymbol{F}_{\pm}(\theta) = -\frac{\Delta\omega}{\langle Z^2 \rangle} \boldsymbol{Z}(\theta + \psi_{\pm}), \tag{15}$$

where the subscripts $+$ and $-$ correspond to the cases $\Omega > \omega$ and $\Omega < \omega$, respectively. Thus, the external force with the minimum energy is proportional to the phase sensitivity function.

The energy of the external force, $P = \langle |\boldsymbol{F}_{\pm}|^2 \rangle$, is given by $P = \Delta\omega^2 / \langle Z^2 \rangle$. The coupling function $\Gamma_{\pm}(\psi)$, corresponding to $\psi_{\pm}$, respectively, is calculated as

$$\begin{aligned} \Gamma_{\pm}(\psi) &= \langle \boldsymbol{Z}(\theta + \psi) \cdot \boldsymbol{F}_{\pm}(\theta) \rangle \\ &= -\frac{\Delta\omega}{\langle Z^2 \rangle} \langle \boldsymbol{Z}(\theta + \psi) \cdot \boldsymbol{Z}(\theta + \psi_{\pm}) \rangle. \end{aligned} \tag{16}$$

The values of $\psi_{\pm}$ can be obtained by solving $\Gamma'(\psi_{\pm}) = 0$. If we define the function as

$$g(x) = \langle \boldsymbol{Z}'(\theta + x) \cdot \boldsymbol{Z}(\theta) \rangle, \tag{17}$$

the condition $\Gamma'(\psi_{\pm}) = 0$ is equivalent to $g(\psi - \psi_{\pm}) = 0$. The following can be demonstrated:

$$g(x + 2\pi) = g(x), \quad g(-x) = -g(x), \quad g(0) = g(\pi) = 0. \tag{18}$$

The first two identities are a consequence of the definition (17), whereas the last identity is derived from the first two identities in Eq. (18). Any pair of (ψ_+, ψ_-) $(\psi_+ > \psi_-)$ that satisfies

$$g(\Delta\psi) = 0, \quad \Delta\psi = \psi_+ - \psi_- \tag{19}$$

constitute a valid solution. In this study, $\psi_- = 0$ is assumed.

2. Case B: Maximum lock-in region of frequency

We considered the external force that provides the maximum frequency lock-in region under the constraint of the constant energy, based on Ref. [31]. The lock-in range $R[\boldsymbol{F}]$ is defined as $R[\boldsymbol{F}] = \Gamma(\psi_+) - \Gamma(\psi_-)$, $\langle |\boldsymbol{F}_{\pm}|^2 \rangle = P$, where P is a constant. The Lagrangian function is $J_*[\boldsymbol{F}] = R[\boldsymbol{F}] - \lambda[\langle |\boldsymbol{F}|^2 \rangle - P]$. The minimizer $\boldsymbol{F}_*$ is

$$\boldsymbol{F}_* = \frac{1}{2\lambda}[\boldsymbol{Z}(\theta + \psi_+) - \boldsymbol{Z}(\theta + \psi_-)], \tag{20}$$

where the value of λ is given by $\lambda = \frac{1}{2}\sqrt{Q/P}$, $Q = \langle [\boldsymbol{Z}(\theta + \psi_+) - \boldsymbol{Z}(\theta + \psi_-)]^2 \rangle$. The coupling function $\Gamma(\psi)$ is

$$\Gamma(\psi) = \frac{1}{2\lambda} \langle \boldsymbol{Z}(\theta + \psi) \cdot [\boldsymbol{Z}(\theta + \psi_+) - \boldsymbol{Z}(\theta + \psi_-)] \rangle. \tag{21}$$

The equation to determine $\psi_{\pm}$ is

$$g(\psi - \psi_+) - g(\psi - \psi_-) = 0, \tag{22}$$

which is obtained by $\Gamma'(\psi) = 0$. Property (18) gives

$$g(\Delta\psi) = 0. \tag{23}$$

3. Case C: Uniform force in spatially localized area

In this paper, we place particular emphasis on the lock-in phenomena induced by a time-periodic external force, denoted $\boldsymbol{f}(\boldsymbol{x}, \Omega t)$, which is spatially uniform and acts within a rectangular area of size $l_x \times l_y$ centered at $\boldsymbol{x}_c = (x_c, y_c)$. Specifically, this is defined as

$$\begin{aligned} &\boldsymbol{f}(\boldsymbol{x}, \Omega t) = \boldsymbol{f}_u(\Omega t) A(\boldsymbol{x}), \quad \boldsymbol{f}_u(\Omega t) = \boldsymbol{f}_u(\Omega t + 2\pi), \\ &A(\boldsymbol{x}) = \begin{cases} 1 & x_c - \frac{1}{2}l_x \leqslant x \leqslant x_c + \frac{1}{2}l_x, \quad y_c - \frac{1}{2}l_y \leqslant y \leqslant y_c + \frac{1}{2}l_y \\ 0 & \text{otherwise.} \end{cases} \end{aligned} \tag{24}$$

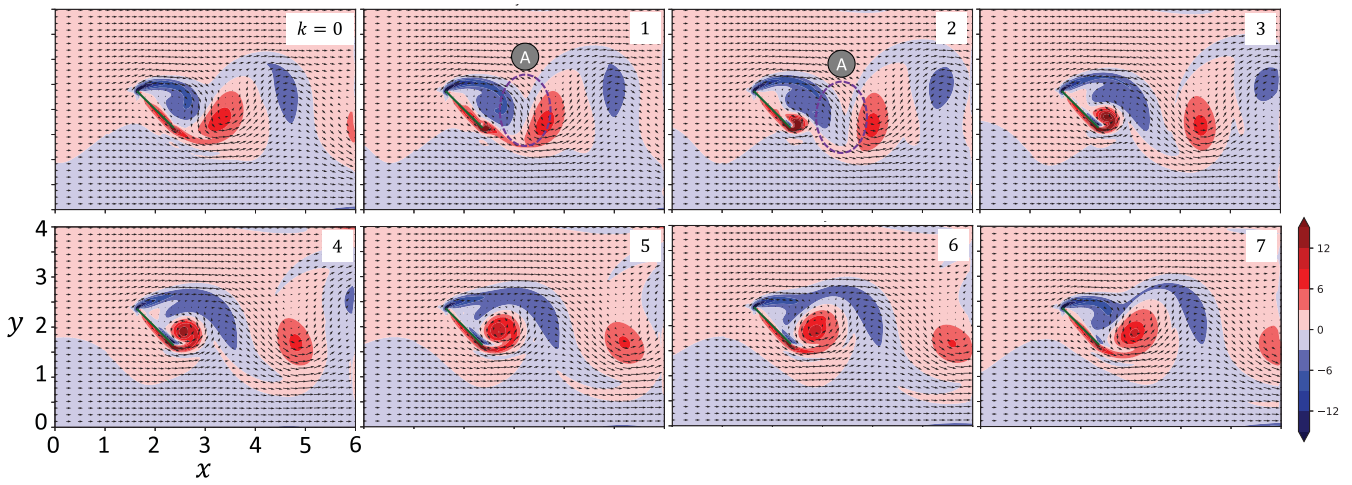

FIG. 2. The velocity and vorticity fields. Snapshots at the phase $\phi/2\pi = k/8$ ($k = 0, 1, \ldots, 7$) are shown.

We highlight the followings key points: (1) In cases where the force is consistently parallel to a constant vector $\boldsymbol{f}_0$, we can describe $\boldsymbol{f}_u(t)$ as

$$\boldsymbol{f}_u(t) = \epsilon f_t(t)\boldsymbol{f}_0. \tag{25}$$

The components of $\boldsymbol{F}(t)$ outside the rectangular area are all zero [cf. Eq. (5)]. Consequently, the coupling function $\Gamma(\psi)$ is solely determined by the values of $\boldsymbol{q}$ within the specified rectangular area.

Finally, to address the optimization problems discussed in Secs. II C 1 and II C 2 for the external force, as defined in Eq. (24), Eqs. (15) and (20) can be used by assuming that the components of $\boldsymbol{Z}$ corresponding to the components of $\boldsymbol{f}$ outside the rectangle to be absent.

Periodic uniform forcing within a spatially localized area is simple, however, the lock-in phenomena of flow past plate for this type of forcing have not been analyzed so far. This type of external forcing can provide a practical flow control strategy. Furthermore, these characteristics above facilitate the design and analysis of the optimal external force, as discussed in Sec. II B the subsequent sections.

III. RESULT

A. Flow and phase sensitivity vector

In this section, the flow details and the phase sensitivity vector field are described, and the optimal external forces for the lock-in phenomena are discussed. In the present condition, the flow converged to a periodic state. The vorticity fields and the flow fields of the periodic solution are shown in Fig. 2, where eight snapshots are shown with equal phase difference, $\phi/(2\pi) = k/8$ ($k = 0, 1, \ldots, 7$).

Leading edge vortex (LEV) and trailing edge vortex (TEV) were generated periodically owing to the uniform flow and their interactions with the plate. The LEV developed ($0 \leqslant k \leqslant 3$) and splits owing to TEV growth ($4 \leqslant k \leqslant 7$). Part of the LEV remains for the redevelopment.

In contrast, TEV develops ($3 \leqslant k \leqslant 6$) to be swept by the flow induced by LEV ($k = 7, 0$) to pinch off ($k = 2$). The volume (area) of the remaining TEV was not as large as that of the LEV, and the main body of the TEV developed near its trailing edge. Thus, major vortex interactions occurred on the rear side of the plate. Figure 3 shows the phase sensitivity vector field $\boldsymbol{q}(\boldsymbol{x}, \phi)$.

The region exhibiting a pronounced phase response to the perturbation [$|\boldsymbol{q}(\boldsymbol{x}, \phi)| > 1.6$] featured a distinctive spatial structure characterized by narrow, curve-like formations. Similar structures of PSF are observed in the case of NACA0012 wing with $Re = 100$ flow [21]. Although the specific configuration of these structures varies with the phases, a typical pattern on the backside of the plate comprises two nearly parallel curve-like structures [e.g., marked as "a" in Fig. 3 ($k = 1$)]. Furthermore, stronger response regions [$|\boldsymbol{q}(\boldsymbol{x}, \phi)| > 3.2$] were primarily observed close to the leading edge, the trailing edge, and the region behind the plate where LEV and TEV interact.

When comparing the vortex dynamics with the structure of the phase response vector, a portion of the influence of $\boldsymbol{q}(\boldsymbol{x}, \phi)$ can be attributed to the evolution of the flow, as outlined below. However, all aspects of the flow evolution are not captured by $\boldsymbol{q}(\boldsymbol{x}, \phi)$. The vortex fields shown in Fig. 2 ($k = 1$) and ($k = 2$) reveals certain features, and only the size of the LEV changes. The TEV flows downward and subsequently pinches off. The flow field situated between LEV and TEV exhibits a negative y direction, indicated by "A" in Fig. 2 ($k = 1$). Region A shifts downstream, as shown in Fig. 2 ($k = 2$). Furthermore, Fig. 3 ($k = 1$) illustrates that the perturbations advance the phase. The structure of the phase sensitivity vector in the negative y flow region weakens the flow in the vicinity of the near-plate part of region A, while it strengthens the flow in the far-plate part. This alternation encourages a change in the flow behavior with respect to that observed at $k = 2$.

Another consequence of $\boldsymbol{q}(\boldsymbol{x}, \phi)$ is a modification in the timing of the separation. The earlier pinch-off of the TEV during Fig. 2 ($k = 1$) and ($k = 2$) occurs when the TEV exhibits more rapid growth. This phenomenon is suggested by the structure of $\boldsymbol{q}(\boldsymbol{x}, \phi)$ located upstream of the trailing edge, denoted by "b" in Fig. 3 ($k = 1$). Unlike the previously mentioned double-curved structure, this region does not exhibit such features.

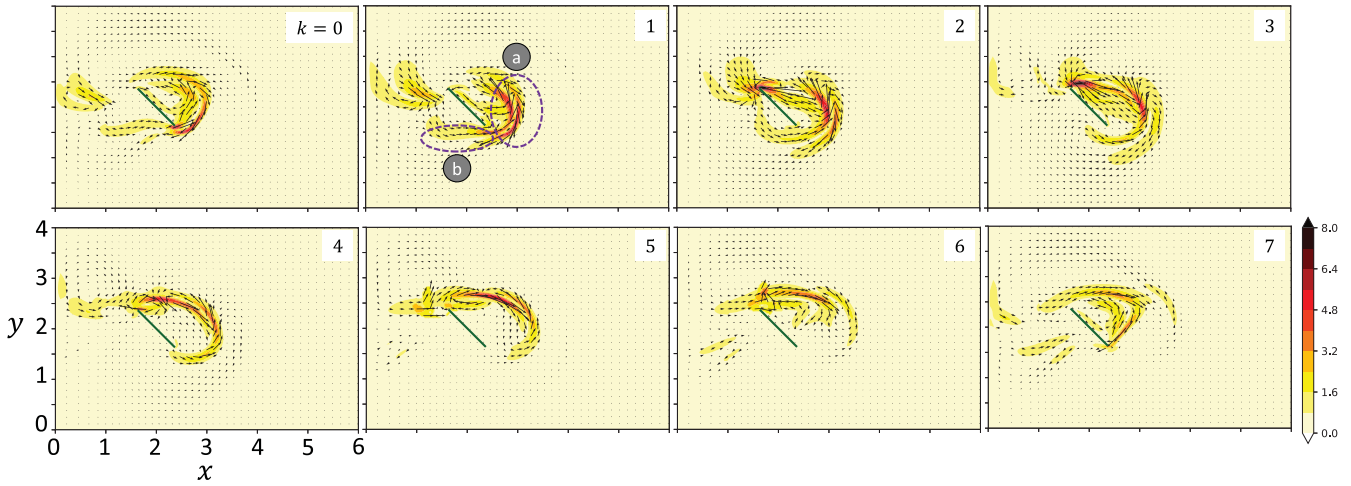

FIG. 3. The fields of the phase sensitivity vector. The contour indicates the magnitude $|\boldsymbol{q}(\boldsymbol{x},\phi)|$. Snapshots at the phase $\phi/2\pi = k/8$ ($k = 0, 1, \ldots, 7$) are shown.

B. Fourier spectrum of phase sensitivity vector

This section discusses the frequency decomposition of the phase sensitivity vector, which is used to examine the frequency-dependent characteristics. As each component of $\tilde{\boldsymbol{q}}(\boldsymbol{x};m) = (\tilde{q}_u(\boldsymbol{x};m),\ \tilde{q}_v(\boldsymbol{x};m))$ represents a field of the complex number, we display $\tilde{q}_j(\boldsymbol{x};m)$ $(i = u, v)$ as a vector in the form of $(\mathrm{Re}[\tilde{q}_j(\boldsymbol{x};m)],\ \mathrm{Im}[\tilde{q}_j(\boldsymbol{x};m)])$. In this presentation, the magnitude of the vector, denoted $|\tilde{q}_j(\boldsymbol{x};m)|$, indicates the strength of the phase sensitivity to sinusoidal perturbations with angular frequency $m\Omega$ [cf. Eq. (13)]. The angle between the vector and the x axis corresponds to $\arg(\tilde{q}_j(\boldsymbol{x};m))$. Notably, the area in which the argument of a complex number is uniform (vectors are parallel) and the magnitude of $\tilde{q}_u(\boldsymbol{x};m)$ [or $\tilde{q}_v(\boldsymbol{x};m)$] is large and regarded constant signifies an area with a relatively pronounced phase response to uniform forcing (see discussions in Sec. II C 3). The response to the perturbation at the angular frequency Ω is depicted in Figs. 4(a) and 4(b). The quantities $\tilde{q}_u(\boldsymbol{x};1)$ and $\tilde{q}_v(\boldsymbol{x};1)$ identify different regions that exhibit a strong response to the periodic perturbation. Specifically, regions with large $|\tilde{q}_u(\boldsymbol{x};1)|$ are predominantly situated downstream of both the leading and trailing edges, whereas regions with large $|\tilde{q}_v(\boldsymbol{x};1)|$ are primarily found downstream of the middle of the plate. In summary, the phases within these regions exhibited relatively minor variations, suggesting that a uniform periodic external force was effective when applied to each of these distinct areas. However, notably, the specific phase values depend on the region, implying that the lock-in phase varies based on the location.

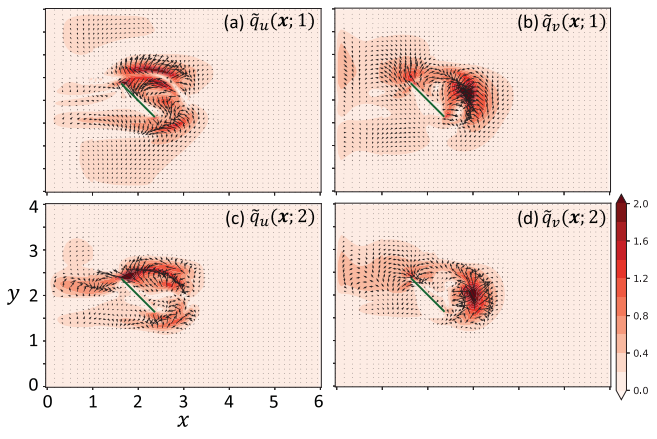

FIG. 4. Phase responses to periodic forcing, $\tilde{q}_u(\boldsymbol{x};m)$ and $\tilde{q}_v(\boldsymbol{x};m)$. Arrows and contours indicate the values (complex numbers in a Gauss plane) and their amplitudes, respectively. (a) $\tilde{q}_u(\boldsymbol{x};1)$, (b) $\tilde{q}_v(\boldsymbol{x};1)$, (c) $\tilde{q}_u(\boldsymbol{x};2)$, (d) $\tilde{q}_v(\boldsymbol{x};2)$.

The response to a perturbation with an angular frequency 2Ω is depicted in Figs. 4(c) and 4(d). The overall magnitude characteristics closely resembled those observed for $m = 1$. However, slight shifts were observed in the specific downstream regions, and the phase changed more rapidly within each area compared with the $m = 1$ scenario. Notably, a broader area upstream of the leading edge was observed where $|\tilde{q}_v(\boldsymbol{x};2)|$ assumed higher values $[|\tilde{q}_v(\boldsymbol{x};2)| > 0.4]$. In Sec. III C, the details of the response are discussed. The response to the perturbation with an angular frequency $m\Omega$ $(m \geqslant 3)$ is depicted in Fig. 5. As the value of m increases, both $|\tilde{q}_u(\boldsymbol{x};m)|$ and $|\tilde{q}_v(\boldsymbol{x};m)|$ decrease in magnitude. Apparently for larger values of m, the region of strong response remained close to the trailing edge, which is a result that the magnitude of PSF is significant at $k = 0$ and 1 in Fig. 3 and almost no contribution at other phases; the magnitude of the PSF's temporal change undergoes a sudden shift.

C. Lock-in details for case C: Uniform periodic external forces in a rectangle region

1. *Where is the best area for largest frequency range of lock-in?*

We consider the frequency lock-in phenomenon induced by uniform periodic external forces within a rectangular region, as defined by Eqs. (24) and (25). Specifically, we concentrate on the scenario where $f_t(t) = \sin mt$, and $\boldsymbol{f}_0 = (1, 0)$ and (0,1), forming a basis of $\mathbb{R}^2$. The sizes of the rectangular areas were selected as $(l_x, l_y) = (1.0, 0.5)$ and $(0.5, 1.0)$, which closely matched those of the regions where $|\tilde{q}_u(\boldsymbol{x};m)|$ or $|\tilde{q}_v(\boldsymbol{x};m)|$ exhibited significant values. By varying the position

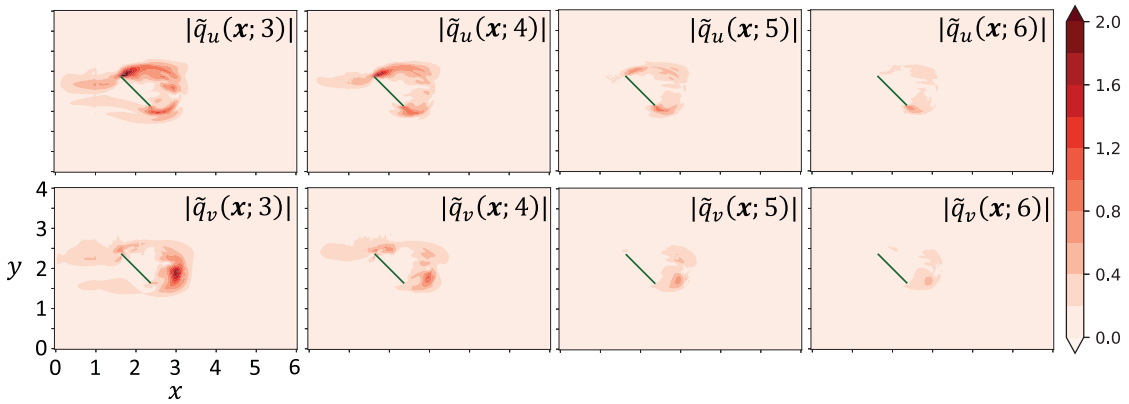

FIG. 5. Amplitudes of phase responses to periodic forcing $|\tilde{q}_u(\boldsymbol{x};m)|$ and $|\tilde{q}_v(\boldsymbol{x};m)|$ $(3 \leqslant m \leqslant 6)$.

vector $\boldsymbol{x}_c$, we derived the scalar field $\Gamma_{\max} = \max_{\psi\in[0,2\pi]}\Gamma(\psi)$ as a function of $\boldsymbol{x}_c$, indicating the extent of the frequency lock-in range.

Hereafter, the scalar field is denoted "$\Gamma^{(m)}_{\max,x}$ for $(l_x, l_y) = (1.0, 0.5)$" [the subscripts "x" and "y" of $\Gamma_{\max}$ denote $\boldsymbol{f}_0 = (1, 0)$ and $\boldsymbol{f}_0 = (1, 0)$, respectively], for instance. Figures 6(a) and 6(b) depict $\Gamma_{\max}$ for $(l_x, l_y) = (1.0, 0.5)$ and $m = 1$ for the external forces in the x and y directions, denoted as $\Gamma^{(1)}_{\max,x}$ and $\Gamma^{(1)}_{\max,y}$, respectively. The chosen rectangular dimensions of 1.0×0.5 roughly resembled the region where $|\tilde{q}_u(\boldsymbol{x};m)|$ is significant. In this context, the field of $\Gamma^{(1)}_{\max,x}$ approximates $|\tilde{q}_u(\boldsymbol{x};m)|$ to some extents. While the rectangle is not similar to the region with large $|\tilde{q}_v(\boldsymbol{x};m)|$, the maximum of $\Gamma^{(1)}_{\max,y}$ is comparable to $\Gamma^{(1)}_{\max,x}$ since the argument of $|\tilde{q}_v(\boldsymbol{x};m)|$ exhibits more uniformity compared with that of $\tilde{q}_u(\boldsymbol{x};m)$. The positions where $\Gamma^{(1)}_{\max,x}$ and $\Gamma^{(1)}_{\max,y}$ attain their maximum values are detailed in Table I, demonstrating these maximum values to be comparable.

Figures 6(c) and 6(d) depict $\Gamma_{\max}$ for $(l_x, l_y) = (1.0, 0.5)$ and $m = 2$. As the phase changes rapidly within regions where $|\tilde{q}_u(\boldsymbol{x};m)|$ or $|\tilde{q}_v(\boldsymbol{x};m)|$ assumes larger values, $\Gamma^{(2)}_{\max,x}$ exhibits smaller values compared with $|\tilde{q}_u(\boldsymbol{x};m)|$ with a few exceptional regions downstream and the upstream of the leading edge. Similar characteristics are observed for the $\Gamma^{(2)}_{\max,y}$ field. While the maximum value of $\Gamma^{(2)}_{\max,x}$ is relatively higher compared with other instances $m = 2$, the peak does not exhibit broader support. Figures 7(a) and 7(b) depict $\Gamma_{\max}$ for $(l_x, l_y) = (0.5, 1.0)$ and $m = 1$. Since the sizes of the rectangle, 0.5×1.0, closely resembles the region where $|\tilde{q}_v(\boldsymbol{x};m)|$ is significant, the $\Gamma^{(1)}_{\max,y}$ field approximates $|q_v(\boldsymbol{x};m)|$ to some extent. However, in this case, the rectangle does not resemble a region with significant $|q_u(\boldsymbol{x};m)|$ values. Notably, the maximum value of $\Gamma^{(1)}_{\max,y}(\simeq 0.21)$ exceeds the maximum value of $\Gamma^{(1)}_{\max,x}$ ($\simeq$0.13; Table I).

Figures 7(c) and 7(d) depict $\Gamma_{\max}$ for $(l_x, l_y) = (0.5, 1.0)$ and $m = 2$. Although the $\Gamma^{(2)}_{\max,x}$ field is generally weak, the $\Gamma^{(2)}_{\max,y}$ field exhibits a prominent peak in the upstream section of the leading edge. The maximum value of $\Gamma^{(2)}_{\max,y}(\simeq 0.10)$ is comparable to the maximum value of $\Gamma^{(2)}_{\max,x}$ for $(l_x, l_y) = (1.0, 0.5)$ (about 0.14). However, the strong region's extent is broader. The broad lock-in region in the upstream of the plate is characteristic of $\Gamma^{(2)}_{\max,y}$ [for both $(l_x, l_y) = (1.0, 0.5)$ and (0.5,1.0)].

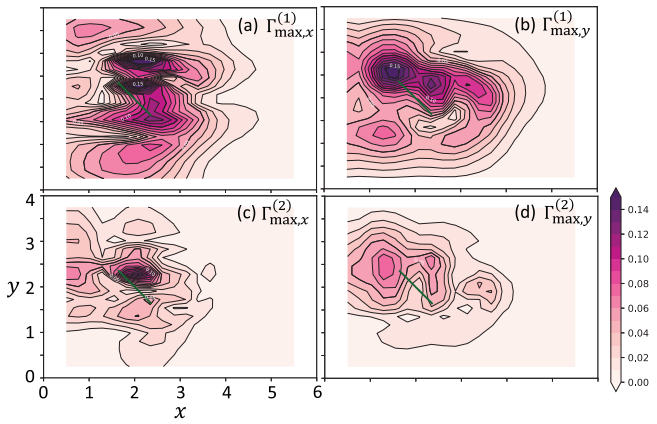

FIG. 6. (a) The field of $\Gamma^{(1)}_{\max,x}$ for $(l_x, l_y) = (1.0, 0.5)$ as a function of $\boldsymbol{x}_c$ [$\boldsymbol{x}^* = (2.079, 2.829)$; cf. Table I]. (b) Same as panel (a), but for $\Gamma^{(1)}_{\max,y}$ [$\boldsymbol{x}^* = (1.553, 2.645)$]. (c) Same as panel (a), but for $\Gamma^{(2)}_{\max,x}$ [$\boldsymbol{x}^* = (2.079, 2.276)$]. (d) Same as panel (c), but for $\Gamma^{(2)}_{\max,y}$ [$\boldsymbol{x}^* = (1.289, 2.645)$].

2. *Arnold tongue: Two cases*

We examine two cases: Cases I and II. (I) Maximizing the lock-in frequency range. We consider $\Gamma^{(1)}_{\max,y}$

TABLE I. The position of rectangle $\boldsymbol{x}^* = (x^*, y^*)$ where maximum frequency lock-in is obtained and the maximum value of $\Gamma_{\max}$.

Mode	(l_x, l_y)	x^*	y^*	Maximum value
$\Gamma^{(1)}_{\max,x}$	(1.0, 0.5)	2.079	2.829	0.1794
$\Gamma^{(1)}_{\max,y}$	(1.0, 0.5)	1.553	2.645	0.1587
$\Gamma^{(1)}_{\max,x}$	(0.5, 1.0)	2.566	1.763	0.1321
$\Gamma^{(1)}_{\max,y}$	(0.5, 1.0)	2.855	2.079	0.2142
$\Gamma^{(2)}_{\max,x}$	(1.0, 0.5)	2.079	2.276	0.1420
$\Gamma^{(2)}_{\max,y}$	(1.0, 0.5)	1.289	2.645	0.07749
$\Gamma^{(2)}_{\max,x}$	(0.5, 1.0)	1.987	2.079	0.07769
$\Gamma^{(2)}_{\max,y}$	(0.5, 1.0)	1.408	2.553	0.1045

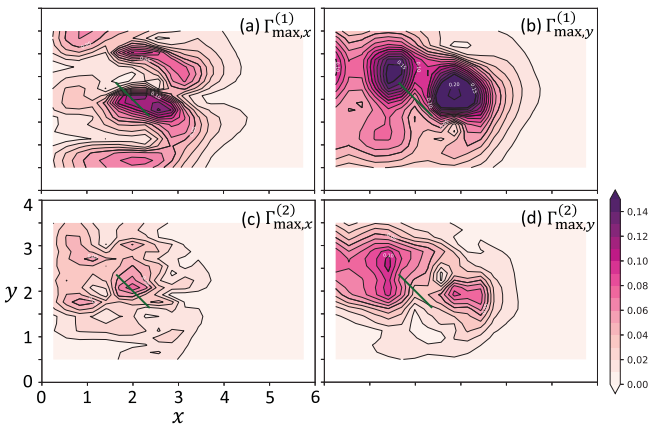

FIG. 7. Same as Fig. 6, but for $(l_x, l_y) = (0.5, 1.0)$. The positions of the rectangles where maximum frequency lock-in is obtained are as follows (cf. Table I): (a) $\boldsymbol{x}^* = (2.566, 1.763)$. (b) $\boldsymbol{x}^* = (2.855, 2.079)$. (c) $\boldsymbol{x}^* = (1.987, 2.079)$. (d) $\boldsymbol{x}^* = (1.408, 2.553)$.

with $(l_x, l_y) = (0.5, 1.0)$. We obtain $\Gamma_{\max} = 0.2142$ where $(x^*, y^*) = (2.855, 2.079)$ (Table I). The rectangular region is located downstream of the plate. (II) Lock-in in the upstream region using an external force. We focus on $\Gamma^{(2)}_{\max,y}$ with $(l_x, l_y) = (0.5, 1.0)$. We obtain $\Gamma_{\max} = 0.1045$ where $(x^*, y^*) = (1.408, 2.553)$ (Table I). Case II corresponds to a $2:1$ frequency ratio lock-in induced by an external force. In addition, the forcing region (rectangle) is situated in the upstream of the leading edge, indicating that the perturbation is advected toward the leading edge, leading to entrainment. A similar large response region in the upstream is reported in the case of the Kármán vortex street [16]. In this sense, this case is interesting although the value of $\Gamma^{(2)}_{\max,x}$ with $(l_x, l_y) = (1.0, 0.5)$ is larger among the examined cases among $m = 2$.

To determine the lock-in region, we conducted direct numerical simulations with periodic external forces for either 500 periods ($\epsilon \geqslant 0.05$) or 1000 periods ($\epsilon < 0.05$). The initial conditions for these simulations were periodic solutions in the absence of external forces. The period of the system under the influence of an external force was determined by the peak-to-peak duration of the lift coefficient. We calculated the average of the last 100 periods to estimate the period and the standard deviation to assess whether frequency lock-in occurs. The angular frequency of the system under the influence of the external force, as obtained through numerical simulation, is denoted $\omega_{\rm sim}$.

To show the change of the aerodynamic characteristics in lock-in states, the relative deviation of the lift coefficient from its nonperturbed state, $\delta = (C_L - C_{L,0})/C_{L,0}$ is also calculated, where C_L and $C_{L,0}$ are the mean lift coefficients with perturbed and nonperturbed states, respectively; the mean values were calculated over the last ten periods of the entire simulation.

Figure 8(a) shows the lock-in region for Case I in the $\Delta\omega$-ϵ plane. The blue triangles represent instances where the frequency lock-in was observed, with the condition: $|\Omega - \omega_{\rm sim}| < \epsilon_e$ where $\epsilon_e = 1.0\times10^{-4}$. Conversely, the gray triangles indicate cases where the frequency lock-in was not observed. The dashed lines delineate the boundary of the lock-in region, as predicted by phase reduction theory [see Eq. (9)] over the entire investigations of $0 \leqslant \epsilon \leqslant 0.15$. The predictions of phase reduction theory align closely with the results from direct numerical simulations. The relative deviation of the lift coefficient δ is indicated by color symbols in Fig. 8(a). The maximum of $|\delta|$ is 0.026. As a general trend, δ is neutral ($|\delta| < 0.005$) when $\epsilon \leqslant 0.025$. When $\epsilon \geqslant 0.05$, δ increases slightly within the lock-in region as ϵ increases, and takes negative or neutral values outside the lock-in region, although some values do not follow. This trend may be comparable to the root-mean-square value of the pressure loss coefficient in fluidic oscillator synchronized by elastic vibration [27].

To examine the details of the lock-in phenomena, we displayed the values of $\Omega - \omega_{\rm sim}$ in Fig. 9 for each ϵ. This representation also highlights the good agreement between the theoretical predictions and the simulation results.

Figure 8(b) shows the lock-in region for Case II in $\Delta\omega$-ϵ plane. In this case, the theoretical predictions closely matches the numerical results when $\epsilon \leqslant 0.05$; however they deviate from each other when $\epsilon > 0.05$. The lock-in range for the region where $\epsilon > 0.05$ shifts to the higher-frequency side as ϵ increases.

For the relative deviation of the lift coefficient δ, the maximum of $|\delta|$ is 0.011 and δ is neutral ($|\delta| < 0.0025$) when $\epsilon \leqslant 0.025$. The trend when $\epsilon \geqslant 0.05$ differs from that in

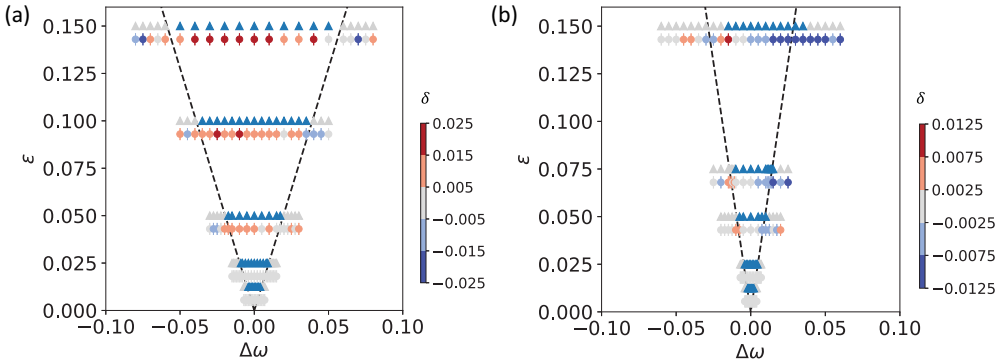

FIG. 8. Arnold tongues. Broken lines indicate theoretical prediction of the lock-in. Blue triangles and gray triangles indicate the lock-in state and no lock-in states, respectively. Relative deviation of the lift coefficient δ is indicated by colored symbols, circle with a vertical line. Vertical positions of the symbols are shifted downward slightly for visibility: (a) Case I, (b) Case II.

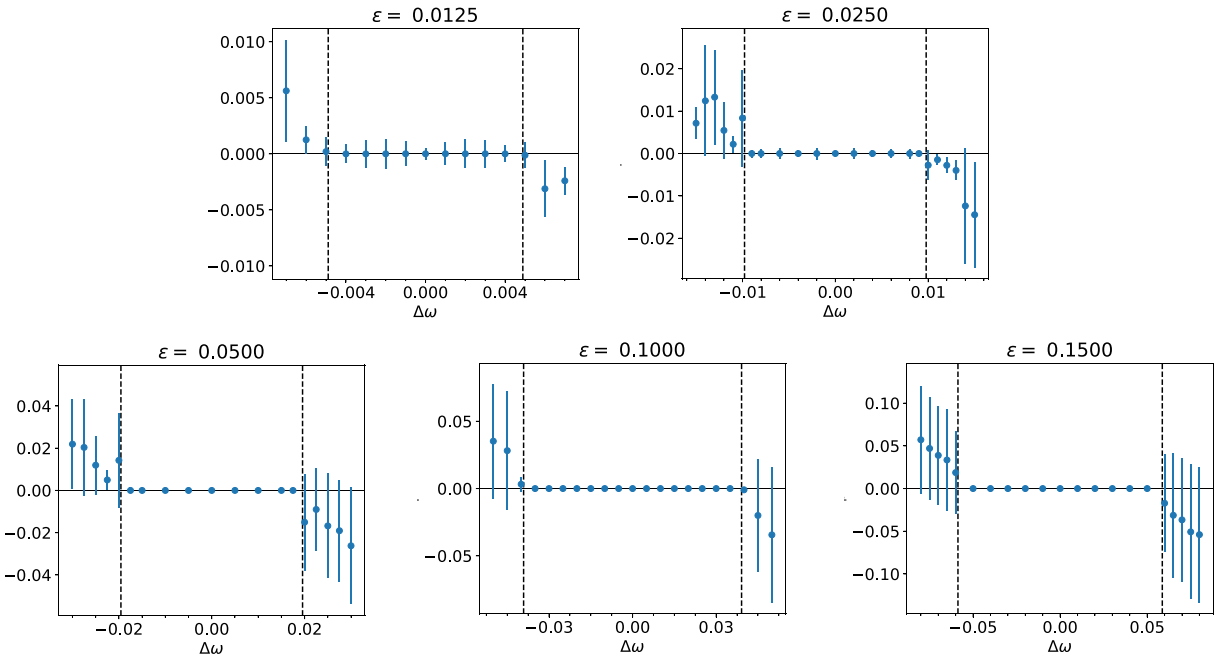

FIG. 9. Difference between the angular frequency of the external force and that observed in the simulation, $\Omega - \omega_{\rm sim}$, for Case I. The points indicate the mean values, with vertical lines representing the standard deviations. Vertical broken lines indicate the theoretical boundary of the lock-in region.

Case I. The value of δ is negative on the higher-frequency side ($\Delta\omega > 0$) and neutral on the lower-frequency side ($\Delta\omega < 0$), although positive values are observed near the boundary of the lock-in region. This trend may be comparable to the maximum value of the pressure-loss coefficient in a fluidic oscillator synchronized by elastic vibration [27].

Examining the details of the lock-in phenomena, we displayed the values of $\Omega - \omega_{\rm sim}$ in Fig. 10 for each ϵ.

D. Optimal external forces that achieves the frequency lock-in and comparison with uniform force within the rectangle region

In this section, the optimal external forces in following two distinct cases are discussed: (A) minimizing the energy of the external force to achieve frequency lock-in, and (B) maximizing the frequency range for lock-in with a constant energy external force. These cases were previously introduced in Sec. II C.

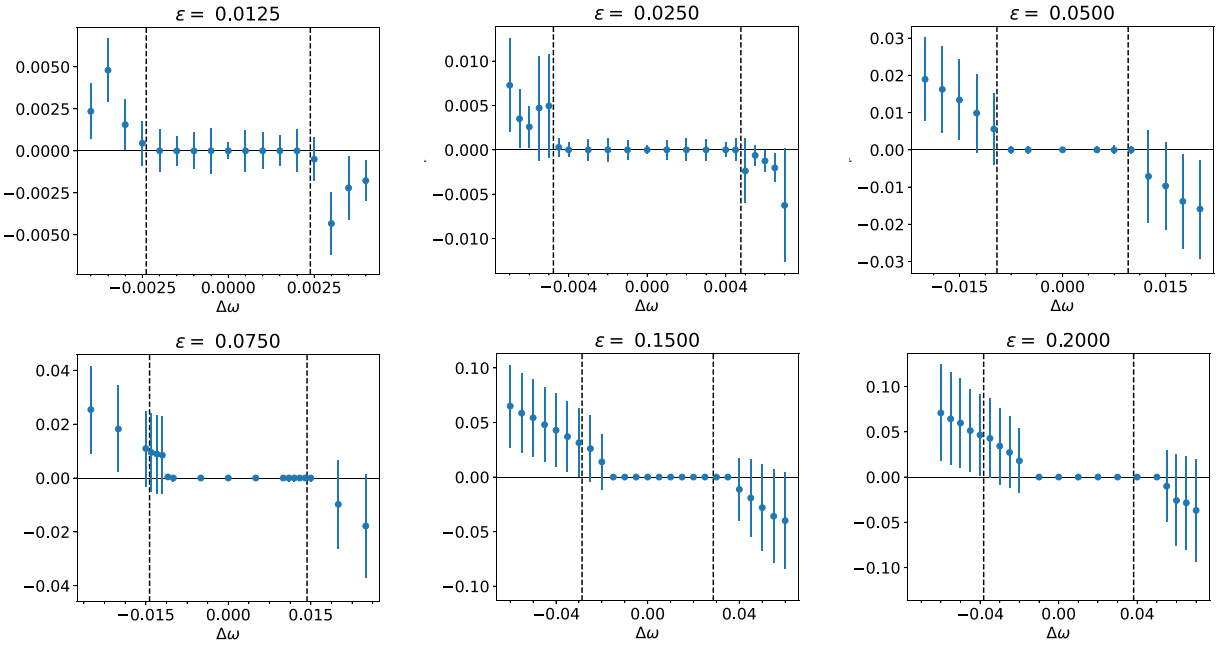

FIG. 10. Same as Fig. 9, but for Case II.

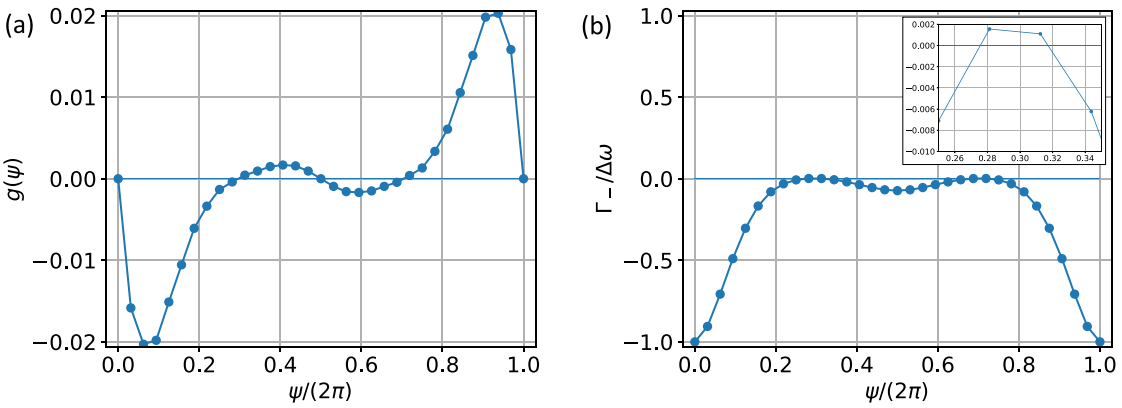

FIG. 11. (a) Graph of the function $g(\psi)$. There are four solutions $\psi = 0,\ \psi^*,\ \pi$, and $2\pi - \psi^*$ for $g(\psi) = 0$. (b) Graph of the function $\Gamma_-(\psi)$. The lowest angular frequency for lock-in is achieved at $\psi = \psi_-(= 0)$.

1. Coupling functions

Regarding Case A, the shapes of the coupling function (16) for $\psi_\pm$ were identical with the only difference of the phase. The phase difference $\Delta\psi$ can be determined from Eq. (19). Assuming $\psi_- = 0$ [Eq. (18)], one of the solutions is $\Delta\psi = \psi_+ = \pi$.

Figure 11(a) shows the function $g(\psi)$. Four solutions were obtained within the region $[0, 2\pi)$, including one nontrivial solution $\psi^*/(2\pi) = 0.2980$ $(\psi^* = 1.0249)$. Notably, $2\pi - \psi^*$ also satisfies the equation according to Eq. (18). Therefore, the complete set of solutions includes: $\psi = 0, \psi^*, \pi$, and $2\pi - \psi^*$.

Figure 11(b) shows the coupling function for $\psi_-(= 0)$ in a nondimensional form by $\Delta\omega$. As expected, the lowest angular frequency for lock-in is achieved at $\psi = \psi_-$. For smaller frequency differences, four lock-in phases were encountered.

Regarding Case B, the coupling functions defined in Eq. (21) were obtained from the solution of Eq. (19). We consider two specific cases $\psi_+ = \pi$, denoted by Γ_1, and $\psi_+ = \psi^*$, denoted by Γ_2. These choices yield distinct coupling functions, which are illustrated in Figs. 12(a) and 12(b), and which we display in a nondimensionalized form by $\frac{1}{2}\sqrt{PQ}$.

Evidently, as shown in Fig. 12(a), the shape of $\Gamma_1(\psi)$ exhibits symmetry with respect to the line $\psi = \pi$. Moreover, the shapes within the ranges $0 \leqslant \psi \leqslant \pi$ and the shape in $\pi \leqslant \psi \leqslant 2\pi$ are antisymmetric with respect to the points $(\psi, \Gamma_1) = (\pi/2, 0)$ and $(\psi, \Gamma_1) = (3\pi/2, 0)$, respectively.

These characteristics can be derived from the definition of Γ_1. In fact, the following two identities hold true: $\Gamma_1(\psi) = \Gamma_1(2\pi - \psi)$ and $\Gamma_1(\psi) = -\Gamma_1(\psi + \pi)$. The first identity can be expressed as follows: The definition of Γ_1 [Eq. (21)] with $\psi_+ = \pi$ and $\psi_- = 0$ implies that $\Gamma_1'(\psi) = \sqrt{P/Q}[g(\psi - \pi) - g(\psi)]$. Then, $\Gamma_1'(\psi) = -\Gamma_1'(-\psi)$ holds due to the properties of $g(\psi)$ [Eq. (18)]. Integrating the relationship, we obtain $\Gamma_1(\psi) = \Gamma_1(2\pi - \psi)$. The second identity can be easily shown through the definition of Γ_1. These two identities indicate that $\Gamma_1(\pi - \psi) = \Gamma_1(2\pi - (\psi + \pi)) = \Gamma_1(\psi + \pi) = -\Gamma_1(\psi)$. Consequently, the following identities hold:

$$\begin{aligned} \Gamma_1(\psi) &= \Gamma_1(2\pi - \psi), \\ \Gamma_1(\pi - \psi) &= -\Gamma_1(\psi), \\ \Gamma_1(2\pi - \psi) &= -\Gamma_1(\pi + \psi), \end{aligned} \tag{26}$$

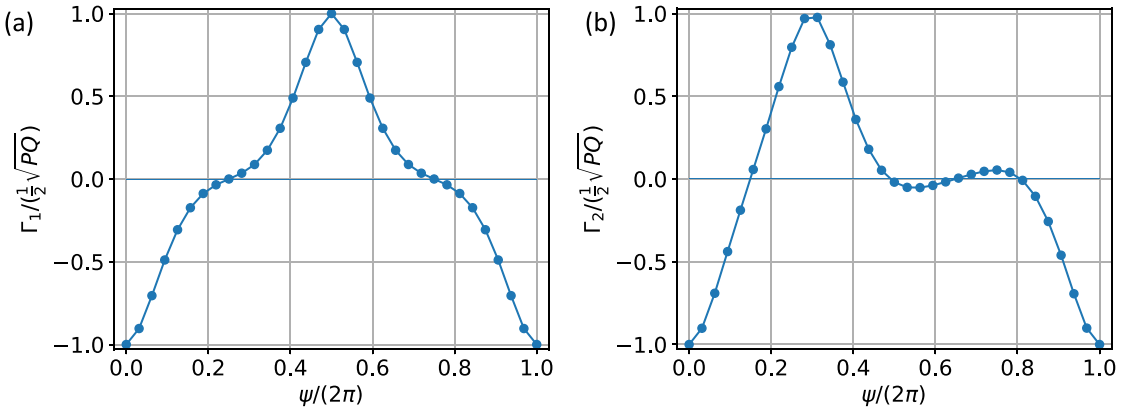

FIG. 12. (a) The graph of the function $\Gamma_1(\psi)$ $(\psi_+ = \pi)$, illustrating symmetries as depicted by Eq. (26). (b) The graph of the function $\Gamma_2(\psi)$ $(\psi_+ = \psi^*)$. There are multiple lock-in phases for smaller frequency difference, $\psi/(2\pi) = 0.491\,649$ and $0.807\,218$.

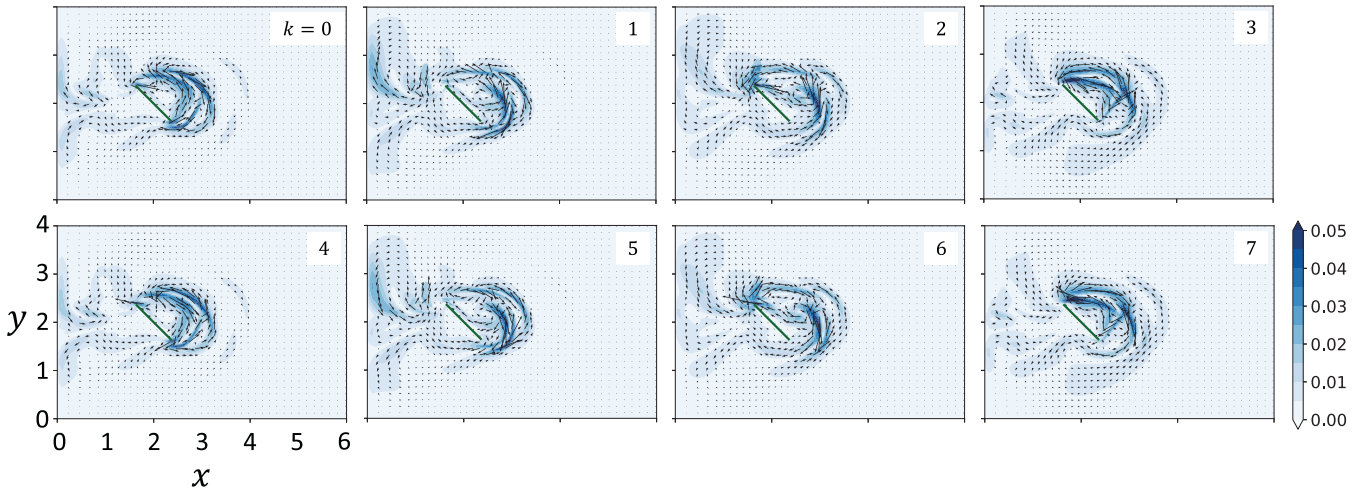

FIG. 13. The fields of the optimal force of the maximum lock-in region, $\boldsymbol{f}_*$, in the case $\psi_+ = \pi$. Arrows and contours indicate the force vectors and their magnitudes, respectively. Snapshots at phase $\theta/2\pi = k/8$ ($k = 0, 1, \ldots, 7$) are shown.

which correspond to the characteristics of Γ_1, as shown in Fig. 12(a).

Based on the properties (26), the lock-in phases for $\Delta\omega = 0$ are $\psi/(2\pi) = 0.25$ (unstable) and 0.75 (stable). The shape of the graph suggests the absence of other lock-in phases.

As shown in Fig. 12(b), the symmetries displayed in Fig. 12(a) are not observed because $\psi_+ \neq \pi$. The shape of $\Gamma_2(\psi)$ can yield multiple lock-in phases for smaller frequency differences within the lock-in region. The stable lock-in phases for $\Delta\omega = 0$ are estimated as $\psi/(2\pi) = 0.491\,649$ and $0.807\,218$ through linear interpolation. We note that the state with two stable lock-in phases is easily lost. Figure 12(b) shows that two stable lock-in phases are lost when $\Delta\omega/(\frac{1}{2}\sqrt{PQ}) < -0.052$ or $\Delta\omega/(\frac{1}{2}\sqrt{PQ}) > 0.054$, although lock-in occurs when $|\Delta\omega| < 1$.

2. Comparison between the uniform force within the rectangular region and optimal forces

In this section, the efficiencies of the uniform force within the rectangular region are discussed by comparing them with the optimal forces. We focus on Case 1, where $\Gamma^{(1)}_{\max,y}$ for $(l_x, l_y) = (0.5, 1.0)$ (referred to as "the case of uniform force" hereafter), and examine the lock-in characteristics in comparison with the optimal forces calculated within the same rectangle region. As previously discussed in Sec. II C 1, the optimal external force is proportional to $-\boldsymbol{Z}(\psi)$ [Eq. (15)]. In the case where the external force is applied only within the rectangular region, the optimal force is determined by using a procedure similar to that described in Sec. II C 1. The optimal external force is given by the Eq. (15) within a localized region.

a. Energy ratio with the same lock-in range. The energy of the external force, $E_{\pm,\mathrm{opt}}$, was obtained from the square of Eq. (15) as $E_{\pm,\mathrm{opt}} = \langle|\boldsymbol{F}_\pm|^2\rangle = \Delta\omega_\pm^2/\langle Z^2\rangle$, where $\Delta\omega_\pm$ corresponds to the cases of $\psi_\pm$, respectively. Notably, $\psi_+/(2\pi) = 0.2606$ when the optimal force is calculated within the rectangle region.

In the case of uniform force, the energy of the external force, E_u, is $E_u = \langle|\boldsymbol{F}_\mathrm{u}|^2\rangle = \epsilon^2 M/2$, where M is the number of grid points within the rectangle. The value of $\langle Z^2\rangle$ is $0.002\,306$ and $M = 450$. Furthermore, as listed in Table I, $\Gamma_{\max} = 0.2142$.

The comparison under the condition that the maximum frequency differences for the lock-in, i.e., $\Delta\omega = \epsilon\Gamma_{\max}$, we obtain

$$\frac{E_{\pm,\mathrm{opt}}}{E_u} = \frac{2\Gamma^2_{\max}}{M\langle Z^2\rangle} = 0.0884. \tag{27}$$

Thus, the energy of external force in the case of uniform force is approximately 8.8% of the optimal energy. Notably, Eq. (27) does not depend on M because $\Gamma \sim M^0$ and $Z \sim M^{-1}$ (cf. Sec. II B).

b. Lock-in range ratio with the same energy. Similar calculation to obtain Fig. 12 provides that the maximum frequency difference of the optimal force within the rectangle region, $\Delta\omega_\mathrm{opt}$, is $\Delta\omega_\mathrm{opt.} = \frac{1}{2}\sqrt{P_\mathrm{opt}Q_\mathrm{opt}}$, where P_opt is the energy of the optimal external force within the rectangular region, and $Q_\mathrm{opt}(= 0.004\,854)$ has the same definition as Q but is calculated within the rectangular region. In the case of uniform force, the maximum frequency difference for the lock-in, $\Delta\omega_\mathrm{rect}$, is $\epsilon\Gamma_{\max}$.

Presumably, the energy of the case of uniform force, E_u, is the same as that of the optimal case, P_opt; i.e., $P_\mathrm{opt} = M\epsilon^2/2$. Then, the ratio of the maximum frequency differences is

$$\frac{\Delta\omega_\mathrm{opt}}{\Delta\omega_\mathrm{rect}} = \frac{0.500\sqrt{MQ_\mathrm{opt}}}{\sqrt{2}\Gamma_{\max}} = 2.44. \tag{28}$$

Thus, the maximum lock-in range for the optimal force is 2.44 times that of the maximum lock-in range for the uniform force.

c. Field of optimal forces. Figure 13 shows the fields of the optimal force of the maximum lock-in region, denoted $\boldsymbol{f}_*(\boldsymbol{x}, \theta)$, in the case $\psi_+ = \pi$. The optimal force is converted to the force field using a similar formula as Eq. (6). Notably,

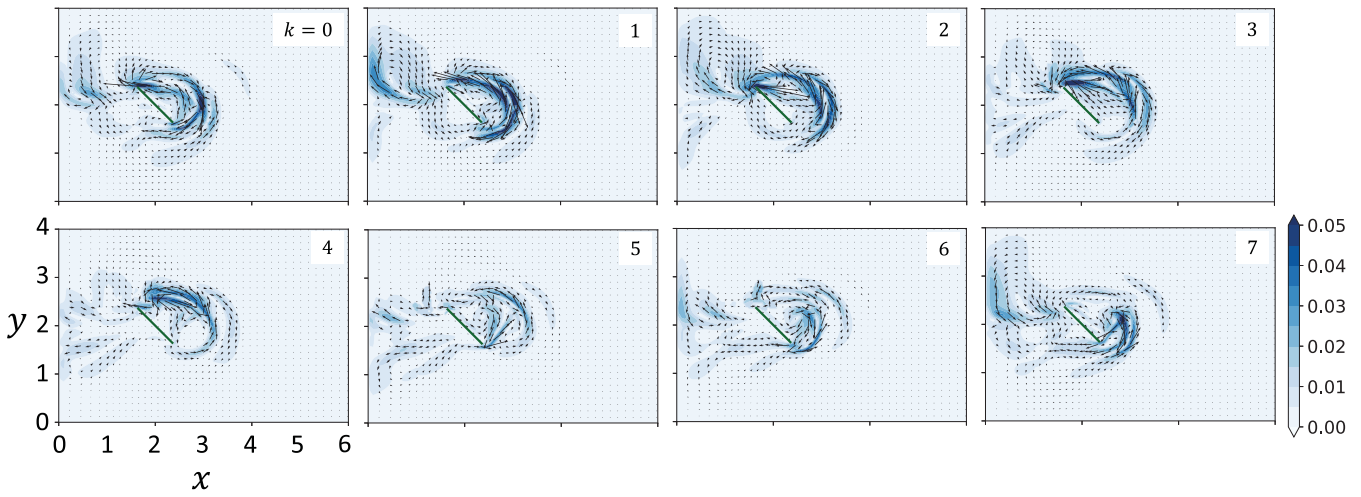

FIG. 14. The fields of the optimal force of the maximum lock-in region, $\boldsymbol{f}_*$, in the case $\psi_+ = \psi^*$. Arrows and contours indicate the force vectors and their magnitudes, respectively. Snapshots at the phase $\theta/2\pi = k/8 (k = 0, 1, \ldots, 7)$ are shown.

the force $\boldsymbol{f}_*(\boldsymbol{x}, \theta)$ satisfies the following relationship:

$$\boldsymbol{f}_*(\boldsymbol{x}, \theta) = -\boldsymbol{f}_*(\boldsymbol{x}, \theta + \pi). \tag{29}$$

This relationship is derived from the definition (21) and the settings of $(\psi_+, \psi_-) = (0, \pi)$. In all the phases, the region with the strongest optimal force is predominantly situated behind the plate. In several phases, such as $k = 1, 2$ (and 5,6), a pronounced region of strong forces is observed upstream of the leading edge, suggesting a more favorable position and timing for the phase control in the upstream region. Figure 14 shows $\boldsymbol{f}_*(\boldsymbol{x}, \theta)$ in the case $\psi_+ = \psi^*$. An area with a strong force $\boldsymbol{f}_*(\boldsymbol{x}, \theta)$ is noticeable when k is between zero and three, rather than when it is between four and seven. Interestingly, the optimal forces for $\psi_+ = \pi$ and ψ^* differ, even though the maximum frequency lock-in region is nearly identical. As shown in Fig. 13, the region with stronger forces is primarily found downstream of the plate, with a noticeable difference between the downstream of the leading edge and that of the trailing edge. This implies that the forces mainly control the interaction between the LEV and TEV to achieve a frequency lock-in. As shown in Fig. 14, a region with stronger forces was observed downstream of the plate and upstream of the leading edge.

IV. SUMMARY

In this study, we applied phase reduction theory to analyze the flow past an inclined plate in a wind tunnel. The thrust was a result of the lock-in phenomenon caused by the external force. We employed the Jacobian-free projection method to calculate the phase sensitivity function, which allowed for an in-depth analysis of its properties. Our examination of the frequency decomposition of the phase sensitivity function revealed a prominent component for modes with $k \leqslant 3$. For mode $k = 2$, we observed a strong response region located in the upstream of the leading edge for the plate.

Building on this knowledge, we investigated the lock-in phenomenon induced by a periodic uniform force applied within a rectangular region. We selected two rectangular regions based on the spatial distribution of the phase sensitivity function and determined the optimal position of the rectangle. Evidently, the optimal position depended on both the mode and the force direction.

Although the primary interactions were observed downstream of the plate, the application of the sinusoidal force in the y direction led to an optimal position upstream of the leading edge for the mode $k = 2$. We then compared the lock-in regions with finite amplitude to the predictions of phase reduction theory. The numerically calculated Arnold tongue indicated that for mode $k = 1$ in the y direction, the result closely matched the theoretical predictions, even for the largest amplitude cases. This alignment suggests that the theoretical assumption of a linear response remains valid even at higher amplitudes. Conversely, for the mode $k = 2$ in the y direction, the agreement was lost, except for the small-amplitude cases. This discrepancy implies that the linearity does not hold as the amplitude increased.

We applied theories that provide optimal external forces for inducing lock-in phenomena and compared the results with those of a detailed investigation of rectangular external forces. These optimal forces can result in multiple lock-in phases, which can be beneficial for future control problems. Furthermore, the optimal forces exhibited distinct features. Cases with multiple phase lock-ins had multiple strong-force regions, both upstream of the leading edge and downstream of the plate. Notably, the multiplicity of strong force regions coincides with multiple phase lock-ins. However, we intend to leave a detailed evaluation of each force regions for future research.

ACKNOWLEDGMENT

This work was partially supported by the Japan Society for the Promotion of Science KAKENHI Grant No. 19K03671 and the SECOM Science and Research Foundation.

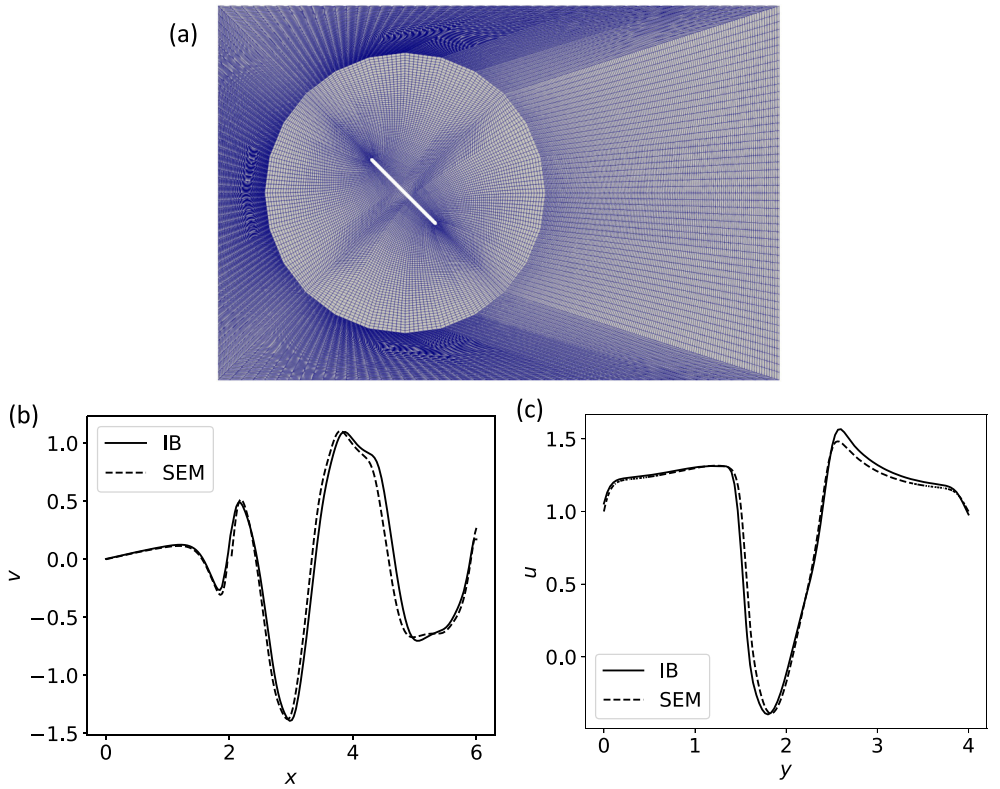

FIG. 15. Comparison with the calculation by the spectral element method.

APPENDIX A: COMPARISON WITH THE SIMULATION BY THE SPECTRAL ELEMENT METHOD

We compared our calculations with those obtained using the open-source program *Semtex*, which employs the spectral element method (SEM) [40,42] to compute the flow around the inclined plate. In SEM, adaptive elements are used to discretize the plate shape and the computational domain, whereas the spectral method is employed to discretize within the elements. In the calculation, we maintained the same computational domain as that in our main calculation, measuring 6×4. However, in the SEM, the plate was modeled with a thickness of $t = 0.04$, and both edges were represented by half circles. The total number of elements in the SEM was 720, and each element was further discretized into 9×9 elements. The computational grid is shown in Fig. 15(a). The boundary conditions at the domain boundary remained consistent with those in our calculations, and the time step was set to 0.001.

We obtained a periodic state through a time evolution calculation in SEM, with a period estimated of 3.461. This value exhibited a discrepancy of less than 1% compared with the period calculated in our main text by the immersed boundary method (IB), 3.440.

Additionally, we examined the v fields by IB and SEM along the line connecting two points, (0,2) and (6,2), as shown in Fig. 15(b). Similarly, we observed the u fields along the line connecting two points, (3,0) and (3,4), as shown in Fig. 15(c). The results showed a reasonable agreement. Notably, discrepancies may arise owing to the discretization method and grid spacing. Furthermore, it is noteworthy that SEM employs a time-evolution calculation, and any differences may be attributed to potential temporal misalignment or a slight error in the selected time.

APPENDIX B: DOMAIN SIZE EFFECT

We compared the phase sensitivity vectors using different domain sizes. As shown in Fig. 16(a), the $\boldsymbol{q}(\boldsymbol{x})$ field was computed with a larger computational domain (8×6) containing 160×160 grid points. To maintain consistency with the main calculation for the computational domain size, we employed the projection method [22] to confine the calculation region to $[2, 8]\times[1, 5]$. The center of the plate was positioned at (4,3) to ensure the relative positioning with respect to the domain for the projection method, as described in the main text. The phase in Fig. 16(a) is at the origin, matching the upper-left image in Fig. 3. Both exhibit similar overall characteristics, and the computed Ritz value is -0.0162, which is sufficiently small, despite the computed area being only half of the entire computational domain.

The velocity fields within both domains are compared along two lines, $y = 3$ and $x = 4.5$, using the coordinate system of the larger computational domain [refer to Fig. 16(a)]. The v component along the line $y = 3$ and the u component along the line $x = 4.5$ are displayed in Figs. 16(b) and 16(c), respectively. The influence of domain size, especially on the width in the y direction, was observed, while the characteristics around the plate remain largely unaffected by the domain.

Figures 16(d) and 16(e) show q_v along the line $y = 3$ and q_u along the line $x = 4.5$, respectively. These figures reveal minimal impact of domain near the plate, although slight

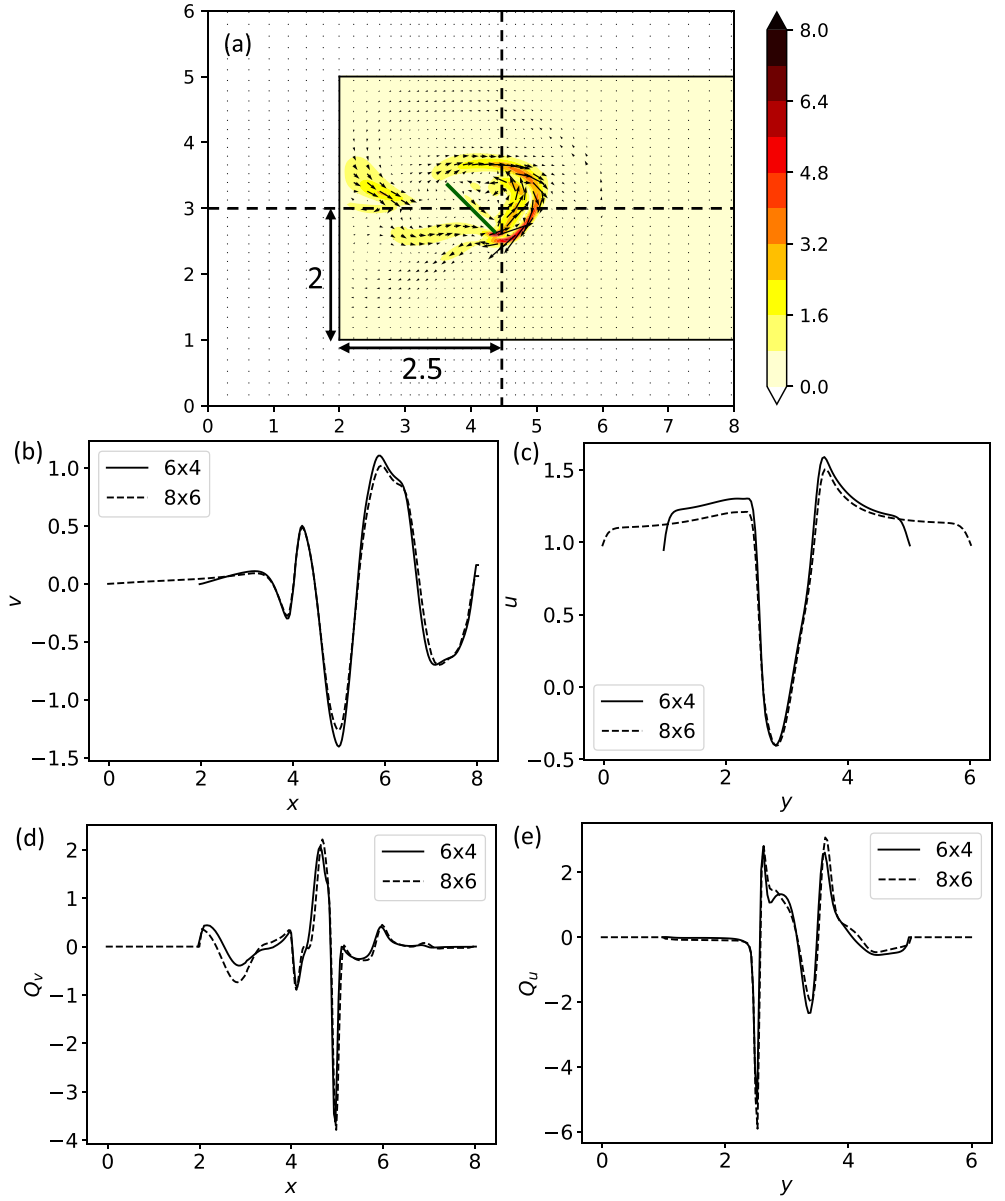

FIG. 16. Comparison with different size of the domain.

differences are noticeable in q_v near the upstream (left) boundary.

Overall, these results indicate that the domain size had an insignificant influence on the calculations in this study.

[1] C. Gao, W. Zhang, X. Li, Y. Liu, J. Quan, Z. Ye, and Y. Jiang, Mechanism of frequency lock-in in transonic buffeting flow, J. Fluid Mech. **818**, 528 (2017).

[2] D. Raveh and E. Dowell, Frequency lock-in phenomenon for oscillating airfoils in buffeting flows, J. Fluids Struct. **27**, 89 (2011).

[3] I. Abroug and N. Abcha, Frequency and phase lock-in behind circular cylinder in the presence of random irregular waves, Phys. Rev. Fluids **7**, 064801 (2022).

[4] C. Williamson and R. Govardhan, Vortex-induced vibrations, Annu. Rev. Fluid Mech. **36**, 413 (2004).

[5] E. de Langre, Frequency lock-in is caused by coupled-mode flutter, J. Fluids Struct. **22**, 783 (2006).

[6] Y. Kuramoto, *Chemical Oscillations, Waves, and Turbulence* (Dover Publications, New York, 1984).

[7] A. Pikovsky, M. Rosenblum, and J. Kurths, *Synchronization: A Universal Concept in Nonlinear Science* (Cambridge University Press, Cambridge, UK, 2001).

[8] J. Pantaleone, Synchronization of metronomes, Am. J. Phys. **70**, 992 (2002).

[9] J. B. Buck, Synchronous flashing of fireflies experimentally induced, Science **81**, 339 (1935).

[10] B. Ermentrout, An adaptive model for synchrony in the firefly *pteroptyx* malaccae, J. Math. Biol. **29**, 571 (1991).
[11] D. Bell-Pedersen, V. M. Cassone, D. J. Earnest, S. S. Golden, P. E. Hardin, T. L. Thomas, and M. J. Zoran, Circadian rhythms from multiple oscillators: Lessons from diverse organisms, Nat. Rev. Genet. **6**, 544 (2005).
[12] A. Asgari-Targhi and E. B. Klerman, Mathematical modeling of circadian rhythms, WIREs Syst. Biol. Med. **11**, e1439 (2018).
[13] Y. Kawamura and H. Nakao, Noise-induced synchronization of oscillatory convection and its optimization, Phys. Rev. E **89**, 012912 (2014).
[14] Y. Kawamura, Phase reduction of limit-torus solutions to partial differential algebraic equations, Phys. Rev. Res. **1**, 033130 (2019).
[15] K. Taira and H. Nakao, Phase-response analysis of synchronization for periodic flows, J. Fluid Mech. **846**, R2 (2018).
[16] M. Iima, Jacobian-free algorithm to calculate the phase sensitivity function in the phase reduction theory and its applications to Kármán's vortex street, Phys. Rev. E **99**, 062203 (2019).
[17] M. A. Khodkar and K. Taira, Phase-synchronization properties of laminar cylinder wake for periodic external forcings, J. Fluid Mech. **904**, R1 (2020).
[18] M. A. Khodkar, J. T. Klamo, and K. Taira, Phase-locking of laminar wake to periodic vibrations of a circular cylinder, Phys. Rev. Fluids **6**, 034401 (2021).
[19] I. A. Loe, H. Nakao, Y. Jimbo, and K. Kotani, Phase-reduction for synchronization of oscillating flow by perturbation on surrounding structure, J. Fluid Mech. **911**, R2 (2021).
[20] A. G. Nair, K. Taira, B. W. Brunton, and S. L. Brunton, Phase-based control of periodic flows, J. Fluid Mech. **927**, A30 (2021).
[21] Y. Kawamura, V. Godavarthi, and K. Taira, Adjoint-based phase reduction analysis of incompressible periodic flows, Phys. Rev. Fluids **7**, 104401 (2022).
[22] M. Iima, Phase reduction technique on a target region, Phys. Rev. E **103**, 053303 (2021).
[23] V. Godavarthi, Y. Kawamura, and K. Taira, Optimal waveform for fast synchronization of airfoil wakes, J. Fluid Mech. **976**, R1 (2023).
[24] H. Gunnoo, N. Abcha, and A. Ezersky, Frequency lock-in and phase synchronization of vortex shedding behind circular cylinder due to surface waves, Phys. Lett. A **380**, 863 (2016).
[25] C. S. Skene and K. Taira, Phase-reduction analysis of periodic thermoacoustic oscillations in a Rijke tube, J. Fluid Mech. **933**, A35 (2021).
[26] T. R. Ricciardi, W. R. Wolf, and K. Taira, Transition, intermittency and phase interference effects in airfoil secondary tones and acoustic feedback loop, J. Fluid Mech. **937**, A23 (2022).
[27] I. A. Loe, T. Zheng, K. Kotani, and Y. Jimbo, Controlling fluidic oscillator flow dynamics by elastic structure vibration, Sci. Rep. **13**, 8852 (2023).
[28] D. Yang, B. Pettersen, H. I. Andersson, and V. D. Narasimhamurthy, Vortex shedding in flow past an inclined flat plate at high incidence, Phys. Fluids **24**, 084103 (2012).
[29] H. Nakao, Phase reduction approach to synchronisation of nonlinear oscillators, Contemp. Phys. **57**, 188 (2016).
[30] V. Novičenko and K. Pyragas, Computation of phase response curves via a direct method adapted to infinitesimal perturbations, Nonlinear Dyn. **67**, 517 (2012).
[31] T. Harada, H.-A. Tanaka, M. J. Hankins, and I. Z. Kiss, Optimal waveform for the entrainment of a weakly forced oscillator, Phys. Rev. Lett. **105**, 088301 (2010).
[32] A. Zlotnik and J.-S. Li, Optimal entrainment of neural oscillator ensembles, J. Neural Eng. **9**, 046015 (2012).
[33] A. Zlotnik, Y. Chen, I. Z. Kiss, H.-A. Tanaka, and J.-S. Li, Optimal waveform for fast entrainment of weakly forced nonlinear oscillators, Phys. Rev. Lett. **111**, 024102 (2013).
[34] H.-A. Tanaka, Optimal entrainment with smooth, pulse, and square signals in weakly forced nonlinear oscillators, Phys. D (Amsterdam, Neth.) **288**, 1 (2014).
[35] H.-A. Tanaka, Synchronization limit of weakly forced nonlinear oscillators, J. Phys. A: Math. Theor. **47**, 402002 (2014).
[36] M. Iima, Phase responses and flow characteristics of a family of Kármán's vortex streets, in *Proceedings of the 2019 International Conference of Nonlinear Theory and its Applications* (IEICE, Tokyo, 2019), pp. 369–372.
[37] S. Dong, G. Karniadakis, and C. Chryssostomidis, A robust and accurate outflow boundary condition for incompressible flow simulations on severely-truncated unbounded domains, J. Comput. Phys. **261**, 83 (2014).
[38] H. Liu and K. Kawachi, A numerical study of insect flight, J. Comput. Phys. **146**, 124 (1998).
[39] M. Uhlmann, An immersed boundary method with direct forcing for the simulation of particulate flows, J. Comput. Phys. **209**, 448 (2005).
[40] H. Blackburn, D. Lee, T. Albrecht, and J. Singh, Semtex: A spectral element-Fourier solver for the incompressible Navier–Stokes equations in cylindrical or cartesian coordinates, Comput. Phys. Commun. **245**, 106804 (2019).
[41] Y. Saiki, Numerical detection of unstable periodic orbits in continuous-time dynamical systems with chaotic behaviors, Nonlinear Proc. Geophys. **14**, 615 (2007).
[42] Y. Fujita and M. Iima, Dynamic lift enhancement mechanism of dragonfly wing model by vortex-corrugation interaction, Phys. Rev. Fluids **8**, 123101 (2023).